



Multiphase superconductivity at the interface between ultrathin FeTe islands and Bi_2Te_3



V. Tkáč^{1,2}, S. Vorobiov^{1,2,3}, P. Baloh^{1,2}, M. Vondráček^{1,4}, G. Springholz^{1,5}, K. Carva¹, P. Szabó³, Ph. Hofmann^{1,6} & J. Honolka^{1,4}

FeTe monolayer islands situated on a topological insulator Bi_2Te_3 (0001) surface were recently reported to exhibit the opening of an energy gap below temperatures $T \sim 6$ K, which could be due to a superconducting phase transition. In this work, we present a magnetic field dependent transport study proving that this gap is indeed of superconducting origin. Upon cooling, several drops in resistance are observed in the temperature range between 6 K and 2 K, indicating multiple transitions. Using the Ginzburg-Landau theory, we show that the critical magnetic field of the dominant high-temperature transition at ~ 6 K is governed by orbital Cooper pair breaking in larger FeTe islands, large enough to exceed the superconductive coherence length ξ . At smaller island sizes, transitions at lower temperatures < 6 K become more prominent, showing significantly increased critical fields dominated by paramagnetic pair breaking. The multiphase superconducting behaviour is in line with an observed wide distribution of FeTe islands width 5–100 nm and seems to reflect disorder effects at the interface to Bi_2Te_3 . The proof of local superconductivity makes the FeTe interface to the topological insulator Bi_2Te_3 substrate a potential host of topological superconductivity.

Interfaces between superconductors and topological insulators (TIs) are predicted to show interesting physics arising from a trivial to non-trivial topology transition, where topological superconductivity (SC) may be realised¹.

The 2008 discovered iron-chalcogenide superconductor family $\text{FeSe}_{1-x}\text{Te}_x$ and respective well-understood Bi-chalcogenide TIs Bi_2Se_3 and Bi_2Te_3 are a promising material combination to study such physics. Both have a simple van der Waals crystal structure consisting of stacked triple (*Ch-Fe-Ch*) and quintuple (*Ch-Bi-Ch-Bi-Ch*) atomic layer units (*Ch* = Te, Se), respectively. In the case of FeCh , one triple layer corresponds to one unit cell (UC) of the respective bulk crystal structure. Throughout the work, 1 UC FeCh will be denoted as a monolayer (ML). FeSe is particularly interesting as its superconducting properties are shown to be highly susceptible to interface effects. The bulk FeSe critical temperature of $T_c = 8$ K² was shown to increase up to 100 K when a single FeSe monolayer (ML) is grown on insulating SrTiO_3 ³. In contrast to FeSe , the parent compound FeTe is at first glance less promising as it is known to exhibit a bi-collinear antiferromagnetic (AFM) order below $T \sim 70$ K and remains non-superconducting in the bulk⁴.

Surprisingly, recent studies of interfaces between FeSe and Bi_2Se_3 turned out not to show SC, while the combination of FeTe and Bi_2Te_3 does. First transport experiments through epitaxially grown *n*-layer thick Bi_2Te_3 on bulk-like FeTe (*n*- Bi_2Te_3 /bulk- FeTe heterostructures) reported values of T_c which depend on the number of Bi_2Te_3 layers and their lateral dimension and reach a maximum $T_c = 12$ K at $n = 7$ ^{5–8}. The superconducting phase is tentatively assigned to unconventional SC triggered by interface-induced charge transfer from FeTe into Bi_2Te_3 topological surface states^{9,10}, which—at the same time—is believed to destroy the FeTe AFM order close to the interface¹¹. Recently, however, Qin et al. reported SC even for $n = 1$ ¹¹ with similar values $T_c \approx 12$ K, which suggests topology not to play a role, as Bi_2Te_3 develops its non-trivial TI properties only at thicknesses $n \geq 2$ ¹². As a complementary approach, inverted (*n*- FeTe /bulk Bi_2Te_3) heterostructures were investigated by scanning tunnelling spectroscopy (STS). In this geometry, TI properties of Bi_2Te_3 can be considered intact, and the FeTe magnetic state is directly accessible via spin-polarised scanning tunnelling microscopy (SP-STM). As highlighted recently by Qin et al.¹³, although SC is expected to emerge at the interface between Bi_2Te_3 and FeTe , the

¹Department of Condensed Matter Physics, Faculty of Mathematics and Physics, Charles University, Prague 2, Czech Republic. ²Institute of Physics, Faculty of Science, P. J. Šafárik University, Park Angelinum 9, Košice, Slovakia. ³Institute of Experimental Physics, Slovak Academy of Sciences, Košice, Slovakia. ⁴Institute of Physics, Academy of Sciences of the Czech Republic, Prague 8, Czech Republic. ⁵Institute of Semiconductor and Solid State Physics, Johannes Kepler University, Altenbergerstrasse 69, Linz, Austria. ⁶Department of Physics and Astronomy, Interdisciplinary Nanoscience Center (iNANO), Aarhus University, Aarhus C, Denmark. e-mail: honolka@fzu.cz

mechanism for SC might be fundamentally different in the inverted approach for single layer FeTe grown on Bi_2Te_3 . Indeed, considerable differences are observed. For 1 ML FeTe ($n = 1$), an energy gap in the local density of states (LDOS) was observed in local STS at temperatures below $T \sim 6$ K, considerably lower than the SC transitions $T_c \sim 12$ K in (n - Bi_2Te_3 /bulk-FeTe) systems¹⁴. This gap is moreover reported to coexist with FeTe bi-collinear AFM order. A trend towards a lower T_c in the inverted approach were recently observed in transport measurements through $\text{FeTe}_{1-y}\text{Se}_y$ monolayers on Bi_2Te_3 when y is reduced from 0.25 to 0.1¹⁵. The disappearance of the gap at much lower temperatures could point to different superconductive properties in (n -FeTe/bulk Bi_2Te_3), but a possible pseudo-gap phase reported, e.g., in high- T_c SCs¹⁶ was so far not ruled out. For a proof of a true superconducting phase, magnetic field dependent studies, e.g. by transport methods, would be needed to extract also characteristic critical fields B_c versus temperature.

In this work, we present a field-dependent transport study on (n -FeTe/bulk Bi_2Te_3) systems, proving a superconducting phase and thus their potential as a host for topological SC. In-plane transport was measured in heterostructures consisting of Si-capped 1–2 ML thick FeTe (FeSe) layers, which were grown on top of molecular beam epitaxy (MBE) fabricated $\text{Bi}_2\text{Te}_3(0001)$ ($\text{Bi}_2\text{Se}_3(0001)$) substrates. The observed transport properties suggest the presence of a non-continuous superconducting state in (n -FeTe/bulk Bi_2Te_3) samples, where the measuring current is flowing through the Bi_2Te_3 substrate between non-percolative superconducting areas of different sizes, causing finite resistance even in the superconducting state. Separated areas are inherently defined by the formation of 60°-rotated tetragonal FeTe island domains on Bi_2Te_3 visible in dark field electron microscopy. At small FeTe coverages of 1 ML, these areas can be extremely small, falling below the superconducting coherence length, which we see as an onset of the paramagnetic Cooper pair breaking regime. Increasing the FeTe coverage to ~ 2 ML, the superconducting phase in FeTe/ $\text{Bi}_2\text{Te}_3(0001)$ becomes more stable with higher critical temperatures of ~ 6 K. Respective critical fields of $B_c \sim 2$ T are attributed to orbital breaking of Cooper pairs with a coherence length $\xi(0)$ of tens of nm, which match the average scale of FeTe island widths.

Results and discussion

Sample fabrication and x-ray photoemission spectroscopy characterisation

For our transport studies, we grew FeCh ($\text{Ch} = \text{Te}, \text{Se}$) layers on respective $\text{Bi}_2\text{Ch}_3(0001)$ surfaces under ultra-high vacuum conditions, following a two-step Fe-deposition and subsequent thermal annealing procedure [see Methods section]. The growth procedure was first described by Cavallin et al. and Manna et al. for bulk Bi-chalcogenide TIs^{14,17}. In order to achieve a higher sensitivity to ultrathin FeCh ($\text{Ch} = \text{Te}, \text{Se}$) layer properties in transport measurements, we here use 300 nm thin MBE-grown $\text{Bi}_2\text{Ch}_3(0001)$ films, which reduces lateral shunt currents through the substrate and fosters

a step-edge induced nucleation and growth process of FeCh monolayer islands¹⁸. Deposited Fe amounts were chosen equivalent to coverages of one and two MLs of FeCh (denoted as “1 ML” and “2 ML” FeCh samples henceforth). For ex situ transport methods, an amorphous Si cap layer was finally added in situ to protect the interface from deterioration in air.

During the different steps of in situ sample preparation, surfaces were thoroughly characterised by x-ray and ultraviolet photoemission spectroscopy. In surface sensitive x-ray photoemission spectroscopy (XPS), the formation of FeCh on $\text{Bi}_2\text{Ch}_3(0001)$ can be traced by the appearance of characteristic chemical shifts in Ch and Bi core levels (CLs)^{18,19}. Figure 1 summarises CL spectra before and after FeCh growth, as well as after Si capping. Te 4d and Se 3d CL contributions originating from the FeTe and FeSe phase (denoted as Te_{Fe} and Se_{Fe} in Fig. 1b, j) are shifted by 0.5 eV and 1.0 eV to higher binding energies (BEs) with respect to those from initial Bi_2Te_3 and Bi_2Se_3 substrate (denoted as Te_i and Se_i in Fig. 1a, i).

The intensity ratios ($\text{Te}_{\text{Fe}}/\text{Te}_i$) and ($\text{Se}_{\text{Fe}}/\text{Se}_i$) of respective components in CLs moreover reflect the FeCh coverage on Bi_2Ch_3 and can be referenced to previously reported XPS data of 1 ML FeCh (thickness 6.3 Å for FeTe and 5.5 Å for FeSe) on top of Bi_2Ch_3 ¹⁸. A shifted Bi 5d CL component at BE ~ 24 eV indicates a partial chemical reaction of Bi_2Ch_3 in line with the reported growth of FeTe as top and embedded islands on Bi_2Te_3 ²⁰. Fe 2p CL shapes in Fig. 1g, o look similar for FeTe and FeSe and are dominated by asymmetric Doniach-Sunjic components (labelled Fe_{DS}) typical for a metallic character of the layer. Contaminations, e.g., from carbon and oxygen, were negligible at all stages of growth.

Study of the electronic band structure

We characterised the electronic band structure and Fermi surface topology of our samples by angle-resolved photoemission spectroscopy (ARPES) techniques. Figure 2 compares ARPES data of 1 ML FeTe (a, b) and 1 ML FeSe (e, f) on $\text{Bi}_2\text{Te}_3(0001)$ and $\text{Bi}_2\text{Se}_3(0001)$, respectively. As references we show ARPES data of in-situ cleaved single-crystalline bulk $\text{Fe}_{1.02}\text{Te}$ (c, d) and $\text{FeSe}_{0.5}\text{Te}_{0.5}$ (g, h) counterparts under the same experimental conditions.

The ARPES Fermi surfaces and LEED patterns of the FeCh MLs (Fig. 2a, e) exhibit the characteristic 12-fold symmetric (k_x, k_y)-space pattern in line with the previously reported formation of three equally prominent 60°-rotated tetragonal FeTe and FeSe island domains (D_1, D_2 , and D_3 hereafter) on the hexagonal $\text{Bi}_2\text{Te}_3(0001)$ and $\text{Bi}_2\text{Se}_3(0001)$ surface symmetry^{18,21}. Dark-field microscopy imaging in Fig. 3a reveals D_1, D_2 , and D_3 domain widths in the range of 5–100 nm, which we approximate by a normal distribution of (50 ± 20) nm.

Exemplary, the Brillouin zones (BZs) of one domain (D_1) and respective \bar{X} and \bar{M} points are sketched in the ARPES Fermi surfaces in Fig. 2a, e. Respective bulk BZs are sketched in Fig. 2c, g, assuming bulk lattice constants $\bar{\Gamma}-\bar{X} = 0.84$ Å⁻¹ ($a' = \pi/3.75$ Å) and $\bar{\Gamma}-\bar{X} = 0.82$ Å⁻¹ ($a' = \pi/3.82$ Å), respectively. The Fermi surfaces of the bulk reference samples in Fig. 2c, g

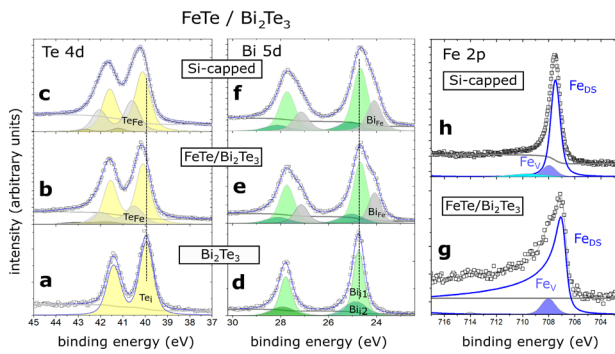
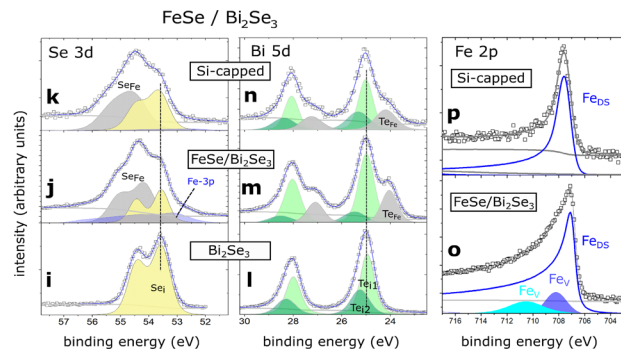


Fig. 1 | Surface sensitive X-ray photoemission spectroscopy characterisation. XPS characterisation during growth of FeTe/ Bi_2Te_3 a–h and FeSe/ Bi_2Se_3 i–p samples. Te 4d, Se 3d and Bi 5d CL spectra, were taken on initial $\text{Bi}_2\text{Ch}_3(0001)$, after 1 ML FeCh growth, and after a-Si capping (bottom, middle, and top panels). Fe 2p CLs after FeTe and FeSe



formation before and after Si-capping are shown in g, h and o, p, respectively. Fits of Te 4d, Se 3d, and Bi 5d CL spectra consist of Voigt-doublet components assuming a Shirley background (grey line). For Fe 2p spectra, asymmetric Doniach-Sunjic profiles (Fe_{DS}) were used. Fitting methods are described in detail in the methods section.

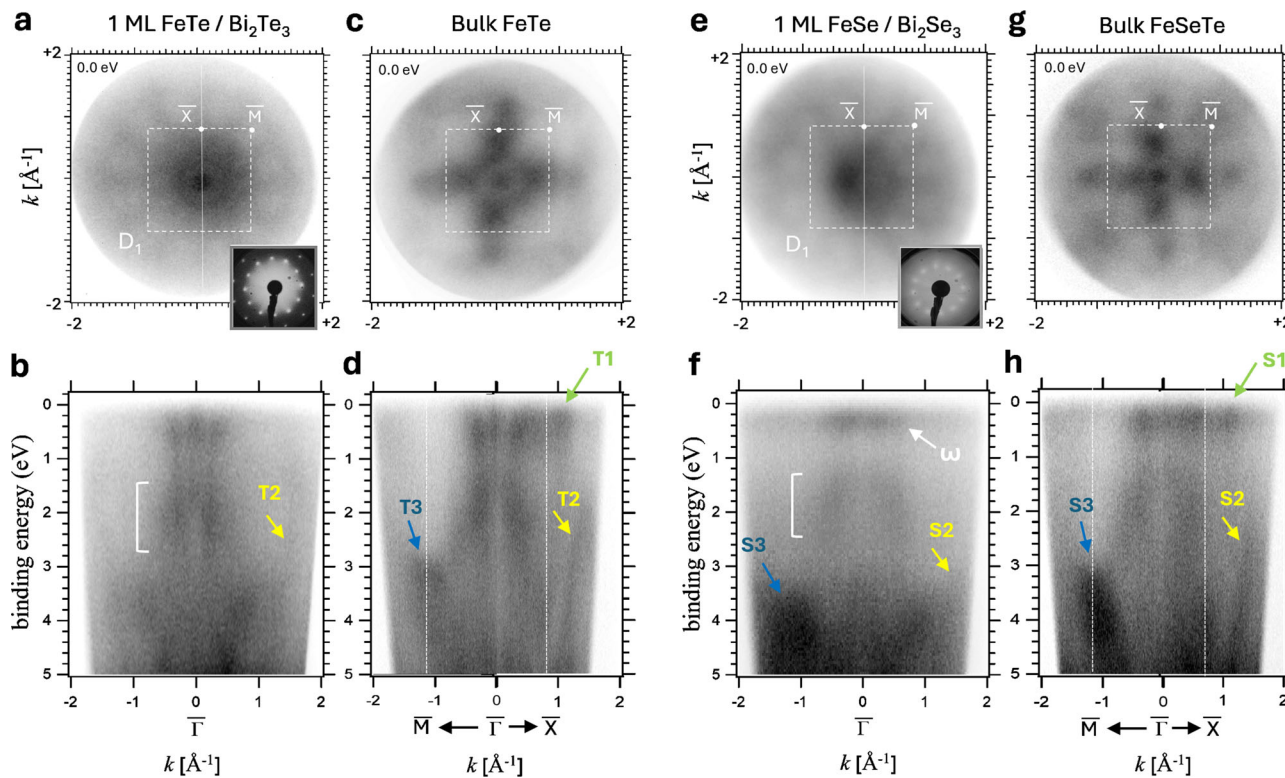


Fig. 2 | Electronic band structure characterisation. Room-temperature ARPES data ($h\nu = 21.2$ eV) of 1 ML FeTe and 1 ML FeSe samples before Si-capping and cleaved bulk FeTe and FeSeTe reference samples. The top row shows the Fermi surfaces and LEED patterns, and bottom row the respective band structures (dark

colour corresponds to high intensity). Left half: Comparison of 1 ML FeTe on $\text{Bi}_2\text{Te}_3(0001)$ **a**, **b** with bulk FeTe **c**, **d**. Right half: Comparison of 1 ML FeSe on $\text{Bi}_2\text{Se}_3(0001)$ **e**, **f** with bulk $\text{FeSe}_{0.5}\text{Te}_{0.5}$ **g**, **h**.

correspond to their tetragonal phase at temperatures well above any known AFM phase transitions in bulk $\text{FeSe}_x\text{Te}_{1-x}$ systems (~ 70 K for FeTe) or tetragonal-to-orthorhombic structural transition in bulk FeSe systems (~ 90 K)². Both Fermi surfaces exhibit a point-like intensity at $\bar{\Gamma}$ and a tetragonal cross-shaped intensity distribution due to higher intensities along $\bar{\Gamma}$ - \bar{X} directions with respect to $\bar{\Gamma}$ - \bar{M} . A broad ARPES intensity at \bar{M} is visible in FeSeTe (Fig. 2g), while in FeTe (Fig. 2c) it is suppressed, all in agreement with earlier reports at photon energies ~ 20 eV and $T \geq 120$ K^{22,23}. The 12-fold azimuthal modulation of the Fermi surface intensity for 1 ML FeTe and 1 ML FeSe at $|k_{\parallel}| \sim 1.2$ \AA^{-1} (Fig. 2a, e) is in line with a superposition of larger intensities along $\bar{\Gamma}$ - \bar{X} directions for each 60°-rotated domain D_1 , D_2 , and D_3 .

Figure 2 (bottom row) compares (k_{\parallel} , E) cuts through 1 ML FeTe and 1 ML FeSe (Fig. 2b, f) as well as bulk FeTe and FeSeTe (Fig. 2d, h). For 1 ML FeTe and 1 ML FeSe \bar{X} - $\bar{\Gamma}$ - \bar{X} cuts through the BZ of D_1 are shown (see vertical lines in Fig. 2a, e). While for single-crystal bulk samples, high-symmetry cuts $\bar{\Gamma}$ - \bar{X} and $\bar{\Gamma}$ - \bar{M} in Fig. 2d, h are well-defined in their BZs, respective cuts through D_1 in 1 ML FeTe and FeSe contain equal contributions also from the 60°-rotated domains D_2 and D_3 . ARPES intensities, therefore, appear averaged, and contain a mixture of bands observed in the respective bulk case along $\bar{\Gamma}$ - \bar{X} and $\bar{\Gamma}$ - \bar{M} directions, e.g. bands indicated T_1 - T_3 [for FeTe] and S_1 - S_3 [for FeSe]. Close to the Fermi surface, bulk and 1 ML data are comparable in the range $|k_{\parallel}| \leq 0.7$ \AA^{-1} . FeSe shows a broad bow-tie-shaped ω -band at 0.25 eV (see label in Fig. 2f) observed also, e.g., for superconductive 1 ML thin FeSe on oxide surfaces²⁴ and a suppressed intensity at higher BEs between 0.5 eV and 1.0 eV²². FeTe on the other hand exhibits the well-known fork-like bands around $\bar{\Gamma}$ ²³, dispersing steeply from the Fermi level to BEs of 1.5 eV with relatively constant intensity. In contrast to 1 ML FeTe, the point-like intensity at $\bar{\Gamma}$ is missing in case of 1 ML FeSe. At higher BEs [1.5 - 2.5] eV broad and strongly dispersing bands appear close to $|k_{\parallel}| \sim 0.5$ \AA^{-1} along $\bar{\Gamma}$ - \bar{X} and $\bar{\Gamma}$ - \bar{M} directions (see white brackets in Fig. 2b, f), as reported earlier in refs. 22,23.

It is important to note that after 1 ML FeCh growth, characteristic band structure features of $\text{Bi}_2\text{Ch}_3(0001)$, such as the topological surface state and prominent downwards dispersing bulk bands starting at ~ 2 eV around $\bar{\Gamma}$ have disappeared (Supplementary Fig. 1a, b and ref. 18). In its initial decapped state, Bi_2Te_3 and Bi_2Se_3 both show the typical intrinsically n-doped behaviour of bismuth chalcogenides (see Supplementary Fig. 1). It confirms the high areal coverage of the $\text{Bi}_2\text{Ch}_3(0001)$ surface by FeCh island domains, in line with our microscopy results in Fig. 3a. We remark that the FeCh coverage dissolves upon annealing to temperatures ≥ 400 °C, where the reappearance of the bare $\text{Bi}_2\text{Ch}_3(0001)$ band structure is observed (see Supplementary Fig. 1c). At these temperatures, the $\text{Bi}_2\text{Ch}_3(0001)$ step-edge assisted nucleation and growth mode of FeCh monolayers (see ref. 18) seems to break down. This is connected to a general loss of surface order evidenced also by the absence of the $\text{Bi}_2\text{Ch}_3(0001)$ topological surface state at $\bar{\Gamma}$.

For ex situ transport measurements, the pre-characterised FeCh/ $\text{Bi}_2\text{Ch}_3(0001)$ surfaces were finally protected by an amorphous Si cap of several nanometre thickness, deposited in situ under UHV conditions at room temperature (see also methods section). In order to monitor the influence of the Si on the ultrathin FeCh layer properties, XPS was once more done at an early stage of the cap deposition process, when the Si thickness was comparable to the XPS probing depth of ~ 10 \AA . Te 4d, Se 3d, and Bi 5d CLs show slight uniform broadening upon Si deposition (see Fig. 1c, k, as well as Fig. 1f, n). Fe 2p CL line shapes in Fig. 1h, p appear sharper and more symmetric, pointing towards a less metallic character of Fe in the presence of the Si interface.

Field-dependent superconductive transport through FeTe layers on $\text{Bi}_2\text{Te}_3(0001)$

Low-temperature superconducting transport measurements Si-cap/FeTe/ $\text{Bi}_2\text{Te}_3(0001)$ and Si-cap/FeSe/ $\text{Bi}_2\text{Se}_3(0001)$ heterostructures were realised by 50 μm silver wire electrodes, which were attached to the Si-capped samples via indium droplets as sketched in Fig. 3a. The sample resistances

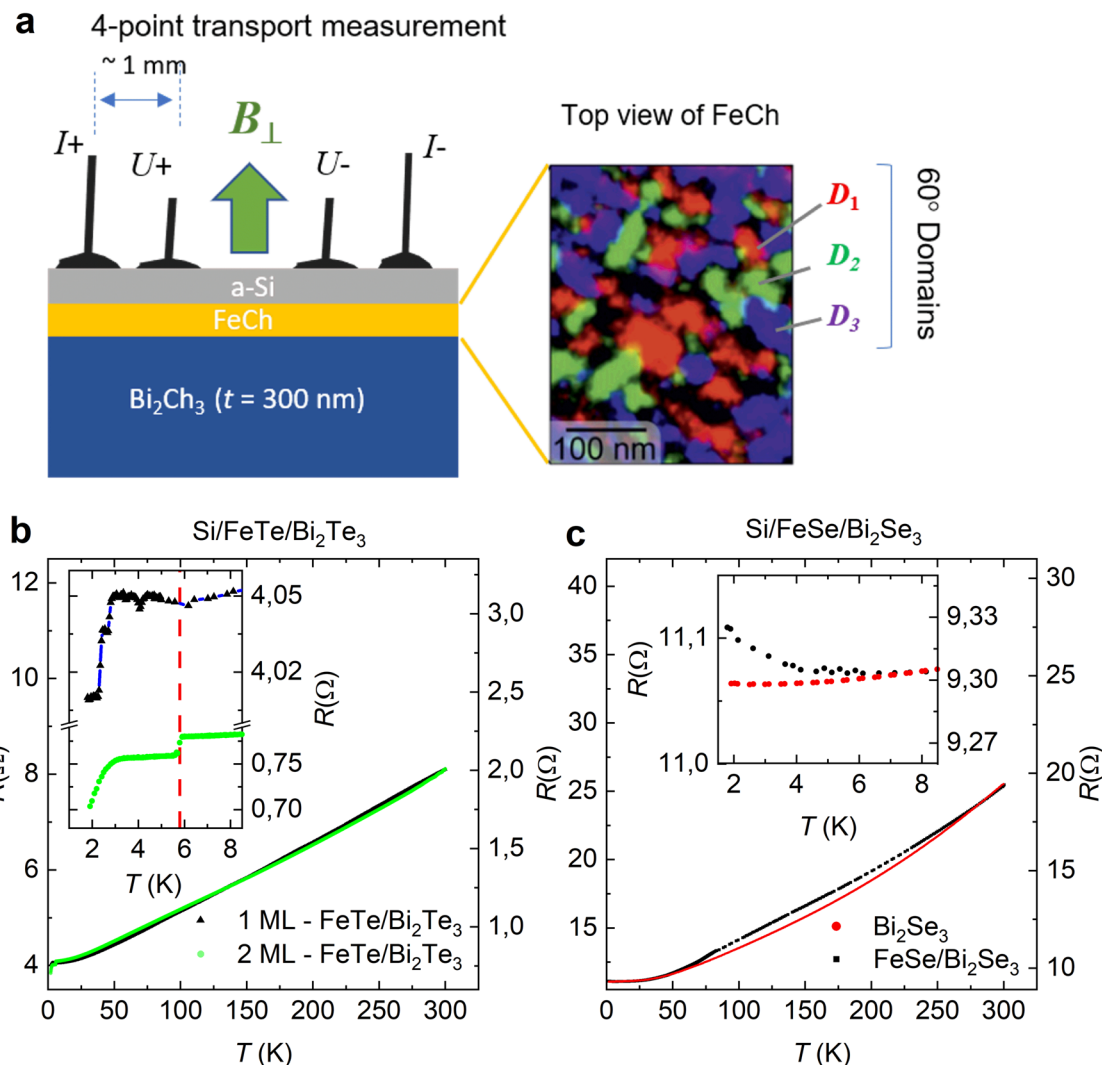


Fig. 3 | Transport measurement set-up and low-temperature resistance at zero field. **a** Left: Schematic view of the 4-point (U^+/U^- , I^+/I^-) transport measurement geometry on Si-capped FeCh/ Bi_2Ch_3 heterostructures. Magnetic fields B_{\perp} (green arrow) are oriented perpendicular to the film. Right: Typical size distribution of 60°-rotated FeSe domains D_1 , D_2 , and D_3 on Bi_2Se_3 (reproduced from ref.¹⁸, CC license 4.0 <https://creativecommons.org/licenses/by/4.0/>). **b** Zero-field temperature dependence of the electrical resistance of Si-capped $\text{FeTe}/\text{Bi}_2\text{Te}_3$ samples with 1 ML

of FeTe (black triangles – left scale) and 2 ML of FeTe (green circles – right scale). Inset: Low-temperature region in detail with multiple resistance drops. The red dashed line marks a transition at about 6 K in both samples. **c** Temperature dependence of the electrical resistance of Si-capped $\text{FeSe}/\text{Bi}_2\text{Se}_3$ sample (black circles – left scale) and – for comparison – a bare Bi_2Se_3 sample (red circles – right scale). Inset: Low-temperature region in detail.

have been determined from the voltage responses (U^+ / U^-) at low bias currents (5 nA to 10 μA) through the leads (I^+/I^-). External magnetic fields were applied perpendicular to the sample plane. We refer the reader to the methods section for further details.

Figure 3 shows the temperature-dependent lateral electrical resistances $R(T)$ measured in zero field on Si-capped 1 ML $\text{FeTe}/\text{Bi}_2\text{Te}_3$ (Fig. 3b–black symbols), 2 ML $\text{FeTe}/\text{Bi}_2\text{Te}_3$ (Fig. 3b—green symbols) and $\text{FeSe}/\text{Bi}_2\text{Se}_3$ (Fig. 3c—black symbols) heterostructures. For comparison, we added a typical $R(T)$ curve of pure Bi_2Se_3 in Fig. 3c (red symbols). Looking at this data at lowest temperatures, the inset of Fig. 3c shows a slight increase of the resistance below 6 K for $\text{FeSe}/\text{Bi}_2\text{Se}_3$ and, much weaker, for Bi_2Se_3 . For Bi_2Se_3 , recent works attribute this rise to increasing electron-electron interactions in the TSS of Bi_2Se_3 at low temperatures²⁵. All $R(T)$ curves in Fig. 3 reveal very similar metallic temperature dependencies down to about 6 K with a residual-resistance ratio $RRR \sim 2$ and saturation below 30 K. At $T \sim 6$ K, a sharp 10% drop in resistance is visible in 2 ML $\text{FeTe}/\text{Bi}_2\text{Te}_3$, which is followed by a more continuous decrease below 3 K (see the inset in Fig. 3b). In the 1 ML $\text{FeTe}/\text{Bi}_2\text{Te}_3$ case, the drop at $T \sim 6$ K (see vertical red line in the inset Fig. 3b) is significantly smaller, while the transition below 3 K now

appears as two rather sharp drops at $T = 2.8$ K and $T = 2.4$ K (total drop amounts to 1%, leveling off at a finite resistance $\sim 4.01 \Omega$). The transition temperatures are best visible on logarithmic temperature scales in Fig. 4a, b. Respective $R(T)$ data of the $\text{FeSe}/\text{Bi}_2\text{Se}_3$ heterostructure shows no sudden drops and approximately follows the curve measured on a pure Bi_2Se_3 sample. Comparing the resistance data obtained on our heterostructures with that of pure Bi_2Se_3 , we can conclude that the order of resistance values of our heterostructures are mainly determined by the respective Bi_2Ch_3 ($\text{Ch} = \text{Te}, \text{Se}$) substrate²⁶.

The multiple drops of the resistances observed in 1 ML $\text{FeTe}/\text{Bi}_2\text{Te}_3$ and 2 ML $\text{FeTe}/\text{Bi}_2\text{Te}_3$ heterostructures at low temperatures point towards the presence of non-percolative low resistance phases formed at the interfaces $\text{FeTe}/\text{Bi}_2\text{Te}_3$ or FeTe/Si . We ruled out a significant role of the FeTe/Si interface for SC, e.g., due to silicide formation^{27,28}, by measuring Si-capped bulk FeTe reference samples where no drops in resistance were observed at temperatures below 40 K (Supplementary Fig. 3). Instead, the resistance drops in our data around 6 K confirms the abovementioned STS studies on $\text{FeTe}/\text{Bi}_2\text{Te}_3$ in the absence of a Si-interface. Local STS on monolayer FeTe reported the formation of energy gaps at critical temperatures $T_c = 6.5$ K and

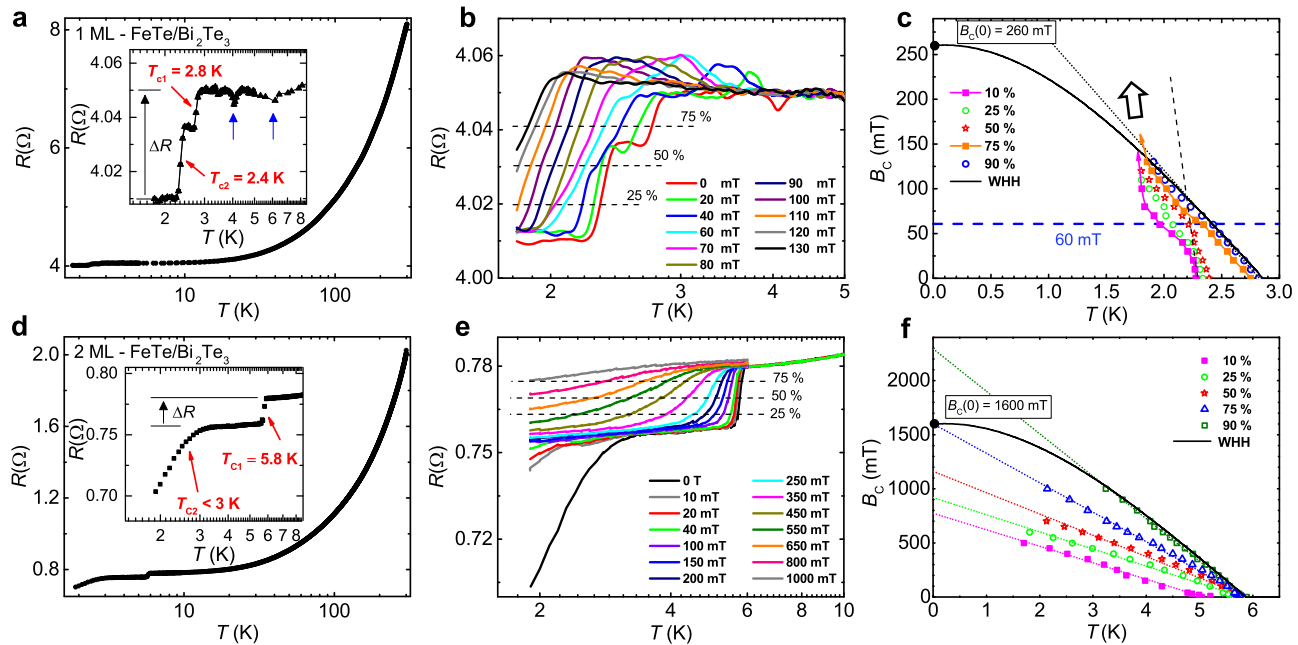


Fig. 4 | Derivation of the critical fields from field-dependent resistance measurements. **a, d** show minor (blue arrows) major (ΔR) steps in the zero-field resistance of Si-capped FeTe/Bi₂Te₃ for 1 ML and 2 ML FeTe coverages. Respective magnetic field-dependent data is shown in **b, e**. For reasons of clarity, the data are not shown for all fields measured. Panels **c** and **f** plot temperature-dependent critical magnetic fields B_c determined from data **b, e** at different percentage levels of the total

drop ΔR . 25%, 50%, and 75% levels are shown as horizontal lines for clarity. Dotted lines fit the linear temperature-dependence characteristic for orbital pair breaking. The black solid lines represent fits according to Werthamer-Helfand-Hohenberg's (WHH) theory with values $B_c(0) = 260$ mT and 1600 mT for 1 ML and 2 ML, respectively. Arrows in **c** are guides to the eye indicating a change towards high critical fields above the blue-coloured $B = 60$ mT line.

$T_c = 7.5$ K for “top” and “embedded” island types, respectively¹⁴. Our observed additional transitions in the temperature range 2–3 K were not reported in STS works at respective temperatures and suggest the existence of even further superconducting phases on a local scale.

To prove the superconducting origin of the observed low-temperature drops in the $R(T)$ curves for FeTe/Bi₂Te₃ heterostructures, we studied their magnetic field dependence. $R(T)$ curves, measured at different fixed magnetic fields B_\perp are shown in Fig. 4, for 1 ML (Fig. 4b) and for 2 ML FeTe heterostructures (Fig. 4e). The drops of the $R(T)$ curves are shifting to lower temperatures with increased magnetic fields, indicative of SC transitions in both cases. Despite the evidence for SC, both sample resistances, however, remain finite down to 1.8 K. The effect of magnetoresistance is negligible in the 1 ML sample, where a small magnetic field of 130 mT was applied (Fig. 4b and Supplementary Fig. 4b). For 2 ML, at much higher fields, a slight shift is visible at 6 K (Fig. 4e) due to magnetoresistance in the normal phase.

Finite values of the resistances below the critical temperature are typical for samples where only small amounts of the material is superconducting and measuring currents are flowing through non-percolative superconducting islands/phases. This is in line with microscopy results in Fig. 3a, where (50 ± 20) nm wide FeTe islands with D₁, D₂, and D₃ orientations seem to be below the percolation limit. We note that also in the case of (n-Bi₂Te₃/bulk-FeTe) heterostructures, a finite resistance is reported when the Bi₂Te₃ coverage reaches the limit $n = 1$ –2, where the percolation limit is expected⁵. In our case, as discussed above, the multiple zero-field resistive transitions at different temperatures (inset Fig. 3b) evidence that these non-percolated islands have varying superconducting properties.

B - T phase diagrams of 1 ML and 2 ML FeTe samples can be derived from the measured field-dependent transport properties. The value of the critical temperature $T_c(B)$ at a fixed magnetic field has been determined from the resistive transitions shown in (Fig. 4b, e). As determination criteria, we used the classical method, where the critical temperature T_c is evaluated at different percentual values of the total resistance step $\Delta R = (R^S - R^N)$ between the normal state resistance (R^N) and the superconducting (R^S) state.

Since our samples did not show zero resistance below the transition temperatures, we considered the plateaus at $R^S = 4.01$ Ω for 1 ML sample and at $R^S = 0.756$ Ω for 2 ML sample as the resistance in the superconducting state as indicated in Fig. 4a, d.

Figure 4c shows the B - T phase diagram of the 1 ML sample for the two well-defined transitions below 3 K. Field-dependent $T_c(B)$ values determined at different percentual levels 10%, 25%, 50%, 75%, and 90% of ΔR are plotted in colours specified in the legend. For clarity, 25%, 50%, and 75% levels are indicated exemplary as horizontal lines in Fig. 4b, e. Points labelled in pink symbols (10% ΔR), green (25% ΔR), and red (50% ΔR), representing mainly the phase with the lowest $T_c \sim 2.4$ K, reveal a rapid increase in the slopes near below T_c (for 10% ΔR the slope is shown as black dashed line in Fig. 4c). Above magnetic fields $B \sim 60$ mT (horizontal blue dashed line), an evident change in their curvature is visible. When the T_c values are determined at higher 75% and 90% ΔR values, the resulting $T_c(B)$ curves correspond to the $T_{c1} = 2.8$ K phase. Even though these curves are closer to a linear dependence, the change in curvature above $B = 60$ mT towards steep slopes is evident (see the black arrow in Fig. 4c). It strongly suggests that the low-temperature phase with $T_c \sim 2.4$ K has a significantly higher critical magnetic field than the phase with $T_{c1} \sim 2.8$ K.

A different behaviour is observed in the respective B - T phase diagram of the 2 ML sample shown in Fig. 4f. Here, $T_c(B)$ curves are quasi-linear for all percentual values 10%, 25%, 50%, 75%, and 90% of ΔR with critical temperatures of ∼5.5–6 K. We comment that we have compensated for the above-mentioned small magnetoresistance effect by shifting the $R(T)$ data in finite fields (Fig. 4e) to match the zero-field data in the normal phase at 6 K. The different linear slopes indicate different B_c values, which reflects the strongly smeared resistive transitions in Fig. 4e in the presence of multiphase superconductivity. The small variation of T_c values between 5.5 K and 6 K derived by linear extrapolation strongly suggests that in transport properties the phase with $T_{c1} = 5.8$ K dominates. We were able to confirm the properties of this superconductive phase independently by magnetic susceptibility measurements giving a consistent critical temperature $T_c = 5.8$ K for the 2 ML sample (see Supplementary Figure 2).

Discussion of the pair breaking mechanism in FeTe and multi-phase superconductivity

In the following, we discuss the B - T phase diagrams of 1 ML and 2 ML samples in the framework of the Ginzburg-Landau theory for type-II superconductors²⁹, considering that Cooper pairs forming the superconducting condensate can be destroyed by orbital or Pauli paramagnetic pair breaking effects.

In the case of orbital pair breaking, the Cooper pairs are broken by superconducting screening currents at the upper critical magnetic field $B_{c2}(0)$, defined as

$$B_{c2}(0) = \frac{\Phi_0}{2\pi\xi(0)^2} \quad (1)$$

where $\Phi_0 = 2.07 \times 10^{-15} \text{ Tm}^2$ is the magnetic flux quantum and $\xi(0)$ is the superconducting coherence length at $T = 0$. For FeSe such critical fields are, e.g., about $\sim 7 \text{ T}$ ³⁰.

Following the Werthamer-Helfand-Hohenberg (WHH) theory³¹, the upper critical magnetic field increases linearly with decreasing temperature and saturates at temperatures close to zero. The saturated value $B_{c2}(0)$ can be estimated from the linear critical field determined from the extrapolation of the linear temperature dependence down to zero in accordance with the expression $B_{c2}(0) = -0.69 T_C |dB_{c2}/dT|_{T_C}$.

When SC is suppressed through a Pauli paramagnetic pair-breaking mechanism, the Zeeman splitting energy of the electronic spins exceeds the superconducting energy gap and destroys the Cooper pair spin ground state. In this case, B_{c2} is recognised as the Pauli-limiting field, defined as

$$B_c^P = \frac{\sqrt{2}\Delta}{g\mu_B} \quad (2)$$

where $g \sim 2$ represents the Landé factor, μ_B the Bohr magneton, and Δ the value of the superconducting energy gap at zero temperature. The value of $B_c^P(0)$ can be estimated in the Clogston limit as $B^P[T] \simeq 1.8T_c [\text{K}]$ ³². The Pauli limiting critical magnetic field reveals a typical square-root temperature dependence $B_c^P \propto (1 - T/T_C)^{1/2}$ at temperatures near T_c .

Which of the pair-breaking mechanisms dominate the suppression of SC in the presence of an applied magnetic field depends on the lateral sample size with respect to the direction of the field. The orbital effects dominate in bulk 3D samples or wide thin films in perpendicular magnetic fields. In the case of nanoscale samples, when the magnetic field is applied in a direction where the sample dimension is smaller than the coherence length ξ , the pair breaking is realised via paramagnetic Zeeman spin-splitting. This is the case in e.g. for ultra-thin films (thickness $< \xi$) in the parallel field or superconducting nanostructures (with dimension $< \xi$).

In the following, we will show that the B - T phase diagrams of 1 ML and 2 ML FeTe samples suggest coverage-dependent contributions from both orbital and paramagnetic pair breaking mechanisms. The different curvatures of the $B_c(T)$ curves of the 1 ML sample derived from different determination criteria (Fig. 4c) indicate the appearance of different pair breaking in the same sample. The huge slope of the $B_c(T)$ curves (black dashed line) and the evidently higher critical magnetic field of the low-temperature phase with $T_{c2} = 2.4 \text{ K}$ strongly suggest the presence of paramagnetic suppression of SC in this phase. On the other hand, the quasi-linear $B_c(T)$ dependencies responsible for the phase with $T_{c1} = 2.8 \text{ K}$ indicate orbital pair breaking, with much lower $B_c \sim 260 \text{ mT}$ (solid black line). The change in curvature of all $B_c(T)$ curves between 60 mT and 100 mT (emphasised by arrows at the end of pink and orange curves), visible regardless of the determination criteria (10–90% ΔR), is due to the flow of measuring current through both phases. Above 150 mT the low temperature phase ($T_{c2} = 2.4 \text{ K}$) with higher (Pauli-limited) critical fields dominates (open black arrow). The observation of both orbital and paramagnetic pair breaking effects in one non-percolative sample is possible only if the sample consists of separate superconducting islands of different widths, of which a large number have sizes smaller than the coherence length.

For the case of orbital pair breaking, the critical field $B_c(0) \sim 260 \text{ mT}$ allows to estimate an in-plane coherence length of $\xi(0) = 36 \text{ nm}$ in the 1 ML case, which indeed only cuts a part of our typical island width distribution of $(50 \pm 20) \text{ nm}$.

For the 2 ML FeTe sample, the B - T phase diagram in Fig. 4f reveals quasi-linear dependences in all $B_c(T)$ curves determined at different determination criteria (10–90% ΔR) and all measured temperatures. Here, the linear slopes change with determination criteria (10–90% ΔR) but converge into the same value $T_{c1} \sim 5.8 \text{ K}$. For the highest slope, we can estimate the value of the zero temperature critical field $B_c(0)$ of 1600 mT again by a WHH fit (solid black line in Fig. 4f). This value is far below the Clogston limit of Pauli pair breaking, which would predict critical fields of approximately 10 T for a superconductor with $T_c = 5.8 \text{ K}$. It confirms the orbital pair breaking mechanism at T_{c1} in the 2 ML case, consistent with the observed linear behaviour of $B_c(T)$. The corresponding coherence length for the critical field 1600 mT corresponds to $\xi(0) = 14 \text{ nm}$, which is close to the low end of the typical distributions of $(50 \pm 20) \text{ nm}$. We comment here that for $(n\text{-Bi}_2\text{Te}_3/\text{bulk-FeTe})$ heterostructures with $n = 7$ considerably smaller values of $\xi(0) = 5.2 \text{ nm}$ were found³, which underlines the possible inequivalence in interface physics of the two approaches.

From the above discussion of field-dependent transport measurements and respective B - T phase diagrams we can conclude the presence of non-percolative multiphase SC in our FeTe/Bi₂Te₃ heterostructures. The multiphase character of the superconducting state in 1 ML and 2 ML samples becomes visible as multiple transitions with different pair-breaking mechanisms, starting at temperatures $T_c \approx 6 \text{ K}$ and continuing below 3 K.

The high-temperature transition at 6 K is most intense at higher FeTe coverages 2 ML and respective critical fields reveal orbital pair-breaking character. This transition compares well to the reported formation of an energy gap at temperatures $T_c = 6.5 \text{ K}$ locally measured by STS in zero field on extended several tens of nanometre wide FeTe monolayer islands on Bi₂Te₃¹⁴. This work's proof of the true superconducting nature of the reported energy gap makes the material system a candidate for the search for topological superconductivity.

Transitions below 3 K, not reported so far, become well-defined at lower FeTe coverages of 1 ML. The temperature dependence of the critical magnetic field of the lowest transition at $T_{c2} = 2.4 \text{ K}$ shows evident multiphase character and a huge increase in B_c near below T_{c2} . We attribute this increase to the presence of paramagnetic pair breaking in extremely small superconducting FeTe islands with lateral dimensions smaller than the coherence length.

The lateral dimensional effects of individual superconducting islands can cause not only different pair-breaking mechanisms and different values of the local critical magnetic field B_c , but also different T_c values. As the dimension of the islands decrease, the mean free path of the charge carriers forming its Cooper pairs decreases, which induces an increase in the electron-electron interaction. This reduces the electronic shielding, enhancing the Coulomb interaction, and leads to suppression of the amplitude of the superconducting wavefunction. Therefore, as the size of a superconducting nanostructure decreases, we can observe a gradual suppression of the energy gap as well as the critical temperature T_c ³³.

Variations in local T_c can, moreover, be caused by local variations in FeTe/Bi₂Te₃ interface properties such as “top” (FeTe van der Waals growth ontop of Bi₂Te₃) and “embedded” (chemical reaction with underlying Bi₂Te₃ during FeTe growth) monolayer island types¹⁴, the nucleation of double-layer FeTe islands even in the nominal 1 ML coverage case²⁰, or the recently observed 2×8 and 1×2 superlattices in the case of van-der-Waals grown FeTe¹³.

Despite the shown unprecedented quantitative values of critical magnetic fields and our interpretation of Cooper pair breaking mechanisms in the framework of Ginzburg-Landau theory, the cause of absence of superconductivity in FeSe/Bi₂Se₃³⁴ and the origin of superconductivity in FeTe/Bi₂Se₃^{9,10,13,35} remain fundamental open questions.

Methods

Sample preparation under UHV conditions

All samples studied in this work were entirely fabricated under UHV conditions (base pressure $p = 5 \times 10^{-11}$ mbar) to ensure clean materials and interfaces. FeCh ($Ch = Te, Se$) layers were grown on respective $Bi_2Ch_3(0001)$ surfaces following a procedure described first by Cavallin et al. and Manna et al.^{14,17} for bulk Bi_2Ch_3 substrates. Here, we use 300 nm thin MBE-grown $Bi_2Ch_3(0001)$ films on insulating $BaF_2(111)$ as substrates. In comparison to bulk surfaces, the choice of MBE-grown $Bi_2Ch_3(0001)$ film substrates fosters a more homogeneous step-flow growth of FeCh monolayers nucleated at densely distributed $Bi_2Ch_3(0001)$ step-edges¹⁸. Clean $Bi_2Te_3(0001)$ and $Bi_2Se_3(0001)$ surfaces were achieved under UHV conditions after the removal of protective (Te, Se) cap layers as described, e.g., in ref. 18.

Fe amounts equivalent to coverages of one, and two monolayers were deposited at room temperature from a calibrated Omicron evaporator. Fe fluxes from an *Omicron* evaporator were calibrated by comparing Fe 2p core level XPS intensities with those of Bi as well as Te or Se. Typical evaporator settings ($I_{Fil} = 1.6$ A, $U = 710$ V, $I_{em} = 10$ mA) resulted in fluxes of ~ 35 nA. Fe coverage estimations by XPS were cross-referenced to STM data of respective Fe growth on clean Au(111).

After Fe deposition, FeTe and FeSe layers form during a 30 min annealing step at temperatures 250 °C and 300 °C, respectively. For ex situ transport methods, an amorphous Si cap layer was finally added in situ to protect the interface from deterioration in air. Si-capping layers were deposited at room temperature from a Si evaporator at 20 cm sample distance at maximum pressures of 1×10^{-9} mbar during deposition.

Photoemission spectroscopy

k-PEEM measurements with laboratory light sources were done at room temperature using an *Omicron NanoESCA* system. The photoemission spectrometer is based on a PEEM column and an imaging double hemispherical energy filter. XPS is done with monochromatised Al K α radiation. Energy-dependent k-space mapping was performed using a helium discharge lamp at $h\nu = 21.2$ eV with an analyser kinetic energy resolution $\Delta E = 0.2$ eV. An overview of the used techniques can be found in ref. 36.

Fitting of core level spectra from XPS and UPS experiments was done in the program *KolXPD* [<https://www.kolibrik.net/kolxpd>]. Bi 5d, Te 4d, and Se 3d were fitted by spin-orbit split Voigt doublets. A Shirley background is assumed in all cases. For Fe 2p spectra, the leading edges are fitted by Doniach-Šunjic profiles.

Low-temperature transport measurements

The samples were glued on a standard *Quantum Design* Helium-3 puck for resistivity measurements with BF-6 glue. Samples were electrically separated from the Helium-3 puck by capacitor paper. Electric contacts were created by 50 μ m silver wires, which were attached to the sample via indium droplets. The droplet was heated at 180 °C for several seconds by gently pressing the soldering tip to the sample surface. This approach ensures good contact through the protective Si layer. Contacts were arranged on the samples in four-point configurations with contact distances of ~ 1 mm.

The electrical ex-situ transport measurements were realised in a *Quantum Design Physical Properties Measurement System* (PPMS) using the AC Transport option in the temperature range from 300 K to 0.4 K in external magnetic fields oriented perpendicular to the plane of the sample and with a minimum current value of $I = 0.01$ mA.

Control measurements were performed with the Resistivity option to exclude possible electric current heating effects at the lowest temperatures with the AC Transport option. The resistivity option allows measuring with a minimum electric current of 5 nA.

Susceptibility measurements

DC susceptibility measurements were performed in *Quantum Design Magnetic Properties Measurement Systems* (MPMS3) in the temperature range from 1.8 K to 10 K in several constant magnetic fields. The sample was

attached to a plastic straw, and the magnetic field was applied perpendicular to the sample plane.

Data availability

Data available on request from the authors.

Received: 10 November 2023; Accepted: 27 June 2024;

Published online: 08 August 2024

References

- Qi, X.-L. & Zhang, S.-C. Topological insulators and superconductors. *Rev. Mod. Phys.* **83**, 1057–1110 (2011).
- Hsu, F.-C. et al. Superconductivity in the PbO-type structure α -FeSe. *Proc. Natl Acad. Sci. USA* **105**, 14262 (2008).
- Ge, J.-F. et al. Superconductivity above 100 K in single-layer FeSe films on doped $SrTiO_3$. *Nat. Mater.* **14**, 285–289 (2015).
- Enayat, M. et al. Real-space imaging of the atomic-scale magnetic structure of $Fe_{1+y}Te$. *Science* **345**, 653–656 (2014).
- He, Q. L. et al. Two-dimensional superconductivity at the interface of a Bi_2Te_3 /FeTe heterostructure. *Nat. Commun.* **5**, 4247 (2014).
- Liu, H.-C. et al. Robust two-dimensional superconductivity and vortex system in Bi_2Te_3 /FeTe heterostructures. *Sci. Rep.* **6**, 26168 (2016).
- He, M. Q. et al. Pseudogap and proximity effect in the $Bi_2Te_3/Fe_{1+y}Te$ interfacial superconductor. *Sci. Rep.* **6**, 32508 (2016).
- Cheng, M. K. et al. Interfacial superconductivity and zero bias peak in Quasi-one-dimensional $Bi_2Te_3/Fe_{1+y}Te$ heterostructure nanostructures. *Adv. Electron Mater.* **9**, <https://doi.org/10.1002aelm.202200943> (2023).
- Yasuda, K. et al. Nonreciprocal charge transport at topological insulator/superconductor interface. *Nat. Commun.* **10**, 2734 (2019).
- Owada, K. et al. Electronic structure of a Bi_2Te_3 /FeTe heterostructure: Implications for unconventional superconductivity. *Phys. Rev. B* **100**, 64518 (2019).
- Qin, H. et al. Superconductivity in single-quintuple-layer Bi_2Te_3 grown on epitaxial FeTe. *Nano Lett.* **20**, 3160–3168 (2020).
- Li, Y.-Y. et al. Intrinsic topological insulator Bi_2Te_3 thin films on Si and their thickness limit. *Adv. Mater.* **22**, 4002–4007 (2010).
- Qin, H. et al. Moiré superlattice-induced superconductivity in one-unit-cell FeTe. *Nano Lett.* **21**, 1327–1334 (2021).
- Manna, S. et al. Interfacial superconductivity in a bi-collinear antiferromagnetically ordered FeTe monolayer on a topological insulator. *Nat. Commun.* **8**, 14074 (2017).
- Moore, R. G. et al. Monolayer superconductivity and tunable topological electronic structure at the $Fe(Se,Te)/Bi_2Te_3$ interface. *Adv. Mater.* **35**, e2210940 (2023).
- Hofmann, J. S., Berg, E. & Chowdhury, D. Superconductivity, pseudogap, and phase separation in topological flat bands. *Phys. Rev. B* **102**, 201112 (2020).
- Cavallin, A. et al. Preparation and characterization of $Bi_2Se_3(0001)$ and of epitaxial FeSe nanocrystals on $Bi_2Se_3(0001)$. *Surf. Sci.* **646**, 72–82 (2016).
- Fikáček, J. et al. Step-edge assisted large scale FeSe monolayer growth on epitaxial Bi_2Se_3 thin films. *New J. Phys.* **22**, 073050 (2020).
- Sánchez-Barriga, J. et al. Observation of hidden atomic order at the interface between Fe and topological insulator Bi_2Te_3 . *Phys. Chem. Chem. Phys.* **19**, 30520–30532 (2017).
- Singh, U. R. et al. Enhanced spin-ordering temperature in ultrathin FeTe films grown on a topological insulator. *Phys. Rev. B* **97**, 144513 (2018).
- Arnold, F. et al. Electronic structure of $Fe_{1.08}Te$ bulk crystals and epitaxial FeTe thin films on Bi_2Te_3 . *J. Phys.: Condens. Matter* **30**, 065502 (2018).
- Nakayama, K. et al. Reconstruction of band structure induced by electronic nematicity in an FeSe superconductor. *Phys. Rev. Lett.* **113**, 237001 (2014).

23. Liu, Z. K. et al. Measurement of coherent polarons in the strongly coupled antiferromagnetically ordered iron-chalcogenide $\text{Fe}_{1.02}\text{Te}$ using angle-resolved photoemission spectroscopy. *Phys. Rev. Lett.* **110**, 037003 (2013).
24. Peng, R. et al. Tuning the band structure and superconductivity in single-layer FeSe by interface engineering. *Nat. Commun.* **5**, 5044 (2014).
25. Tkáč, V. et al. Influence of an anomalous temperature dependence of the phase coherence length on the conductivity of magnetic topological insulators. *Phys. Rev. Lett.* **123**, 036406 (2019).
26. Chiatti, O. et al. 2D layered transport properties from topological insulator Bi_2Se_3 single crystals and micro flakes. *Sci. Rep.* **6**, 27483 (2016).
27. Bernardini, F. et al. Iron-based superconductivity extended to the novel silicide LaFeSiH. *Phys. Rev. B* **97**, 100504 (2018).
28. Bhattacharyya, A. et al. Evidence of nodal superconductivity in LaFeSiH. *Phys. Rev. B* **101**, 224502 (2020).
29. Tinkham, Michael. *Introduction to Superconductivity: Second Edition*. (Courier Corporation, 2004, 2014).
30. Farrar, L. S. et al. Suppression of superconductivity and enhanced critical field anisotropy in thin flakes of FeSe. *NPJ Quantum Mater.* **5**, 29 (2020).
31. Werthamer, N. R., Helfand, E. & Hohenberg, P. C. Temperature and purity dependence of the superconducting critical field, H_{c2} . III. Electron spin and spin-orbit effects. *Phys. Rev.* **147**, 295–302 (1966).
32. Clogston, A. M. Upper limit for the critical field in hard superconductors. *Phys. Rev. Lett.* **9**, 266–267 (1962).
33. Trivedi, N. SuperConductor-insulator Transitions: Present Status And Open Questions. in *Conductor-Insulator Quantum Phase Transitions* 329–351 (Oxford University Press, 2012). <https://doi.org/10.1093/acprof:oso/9780199592593.003.0010>.
34. Eich, A. et al. Absence of superconductivity in ultrathin layers of FeSe synthesized on a topological insulator. *Phys. Rev. B* **94**, 125437 (2016).
35. Yi, H. et al. Dirac-fermion-assisted interfacial superconductivity in epitaxial topological-insulator/iron-chalcogenide heterostructures. *Nat. Commun.* **14**, 7119 (2023).
36. Vondráček, M. et al. Nanofaceting as a stamp for periodic graphene charge carrier modulations. *Sci. Rep.* **6**, 23663 (2016).

Acknowledgements

We thank Prof. M. Bremholm from Aarhus University for the growth of single crystalline bulk FeTe reference samples supported by VILLUM FONDEN via the Centre of Excellence for Dirac Materials (Grant No. 11744). This work was supported by the Czech Science Foundation (Project No. GA22-04408S) and through the project Quantum Materials for Applications in Sustainable Technologies (QM4ST), funded as project No. CZ.02.01.01/00/22_008/0004572 by Programme Johannes Amos Comenius, call Excellent Research. P.Sz. was supported by APVV-18-0358 project, European

Microkelvin Platform, EU ERDF (European regional development fund) Grant No. VA SR ITMS2014 + 313011W856 and VEGA 1/0743/19. G.S. acknowledges support by the Austrian Science Funds (FWF) (Projects P30960-N27 and I4493-N) and LIT-2022-11-SEE-131 of the University of Linz. V.T. was also supported by the Slovak Research and Development Agency Projects numbers APVV-18-0197, APVV-20-0425 and APVV-22-0172.

Author contributions

V. Tkáč, S. Vorobiov, and P. Baloh contributed with electrical sample contacting and transport measurements. M. Vondráček and J. Honolka contributed with sample growth, XPS/ARPES measurements, and manuscript writing. K. Carva performed DFT calculations. P. Szabó contributed with data analysis and manuscript writing. G. Springholz and Ph. Hofmann provided MBE-grown Bi_2Te_3 films and bulk Bi_2Te_3 , respectively.

Competing interests

The authors declare no competing interests

Additional information

Supplementary information The online version contains supplementary material available at <https://doi.org/10.1038/s41699-024-00480-x>.

Correspondence and requests for materials should be addressed to J. Honolka.

Reprints and permissions information is available at <http://www.nature.com/reprints>

Publisher's note Springer Nature remains neutral with regard to jurisdictional claims in published maps and institutional affiliations.

Open Access This article is licensed under a Creative Commons Attribution 4.0 International License, which permits use, sharing, adaptation, distribution and reproduction in any medium or format, as long as you give appropriate credit to the original author(s) and the source, provide a link to the Creative Commons licence, and indicate if changes were made. The images or other third party material in this article are included in the article's Creative Commons licence, unless indicated otherwise in a credit line to the material. If material is not included in the article's Creative Commons licence and your intended use is not permitted by statutory regulation or exceeds the permitted use, you will need to obtain permission directly from the copyright holder. To view a copy of this licence, visit <http://creativecommons.org/licenses/by/4.0/>.

© The Author(s) 2024